2025

Protocol optimization and volumetric imaging for the functional lung atlas

BOSTON UNIVERSITY

COLLEGE OF ENGINEERING

Thesis

PROTOCOL OPTIMIZATION AND VOLUMETRIC IMAGING FOR THE FUNCTIONAL LUNG ATLAS

by

MITCHELL JONES

B.A., Boston University, 2025

Submitted in partial fulfillment of the

requirements for the degree of

Master of Science

2025

Approved by

First Reader

Hadi T. Nia, Ph.D.
Assistant Professor of Biomedical Engineering
Assistant Professor of Materials Science and Engineering

Second Reader

Béla Suki, Ph.D.
Professor of Biomedical Engineering
Professor of Materials Science and Engineering

Third Reader

David A. Boas, Ph.D.
Arthur G. B. Metcalf Chair
Professor of Biomedical Engineering
Professor of Electrical and Computer Engineering

ACKNOWLEDGMENTS

I would like to thank everyone in the Nia lab for their teaching, guidance, and support during this work. These friendships as well as others I've made while in Boston have been invaluable. Hadi, thank you for your mentorship, guiding my growth as a scientist and engineer, as well as for your excitement for this project. To my committee, Dr. Suki and Dr. Boas, as well as all the professors who have taught me at BU, thank you for your guidance and wisdom. To Dr. Boas and Anna Novoseltseva, thank you for generously teaching and allowing our lab to use your facilities. Finally, thank you to my parents and family for their continued love and support from across the country.

PROTOCOL OPTIMIZATION AND VOLUMETRIC IMAGING FOR THE FUNCTIONAL LUNG ATLAS

MITCHELL JONES

ABSTRACT

Understanding how mechanical and pathological forces interact with the 3D lung structure, cellular populations, and molecular architecture on an organ-wide scale remains a central challenge in pulmonary biology and disease research. Current techniques used to spatially interrogate biology — including histology, medical imaging, and spatial transcriptomics — lack the ability to resolve full 3D organ architecture while simultaneously capturing cellular and molecular information. Additionally, live organ imaging methods such as intravital windows and, in our lab, the Crystal Ribcage have enabled impressive visualization of dynamic processes on the lung surface while preserving physiological function, but visuals are restricted to superficial layers due to light scattering. Emerging techniques using chemical optical clearing have overcome this limitation by matching tissue refractive index and removing light-scattering components in fixed tissues, enabling deep optical imaging across intact organs. Additionally, novel cyclic immunofluorescent multiplexing methods have enabled imaging of many molecular targets within a single sample, though labeling thick tissue sections remains a key challenge. Utilizing these advances, this thesis aims to develop a pipeline for volumetric imaging of the murine lung by integrating serial tissue sectioning, 2,2-thiodiethanol (TDE) optical clearing, and high-resolution confocal microscopy. We focused on (1) optimizing sample preparation, clearing, and imaging for thick, well-

oriented lung sections; and (2) aligning slice images to form a complete volume. In part this required registering fluorescent images to a structural scan acquired via section tomography combined with optical coherence tomography, allowing correction of slice deformation and enabling reconstruction of anatomically accurate volumes. This work demonstrates the desired image resolution and alignment for building a functional lung atlas — an integrated 3D map of structural, cellular, and molecular features across the murine lung. Future work will focus on scaling up computation and optimizing multiplex labeling.

TABLE OF CONTENTS

LIST OF FIGURES

LIST OF ABBREVIATIONS

BU ..... Boston University

CT ..... Computed Tomography

cyCIF..... cyclic Immunofluorescence

EGFP..... Emerald Green Fluorescent Protein

IACUC ..... Institutional Animal Care and Use Committee

IBEX ..... Iterative Bleaching and staining

NA..... Numerical Aperture

OCT..... Optical Coherence Tomography

PBS ..... Phosphate Buffered Saline

PDMS..... Poly-Dimethyl Siloxane

PET ..... Positron Emission Tomography

TDE..... 2,2' Thiodiethanol

WT ..... Wild Type

2D..... Two-Dimensional

2P ..... Two-Photon

3D..... Three-Dimensional

4i ..... indirect immunofluorescence imaging

CHAPTER ONE: INTRODUCTION AND RESEARCH AIMS

Introduction

The lung is a highly dynamic organ, continuously subjected to mechanical deformation from respiratory cycles and pulsatile blood flow, while also experiencing a range of biological and immunological stresses. These include infectious and inflammatory stresses, obstructive and restrictive lung diseases, and both primary and metastatic cancers. Understanding how these mechanical and pathological forces interact with the structure and function of the lung — at both the organ and cellular levels — remains a central challenge in pulmonary biology and disease research. Traditional two-dimensional (2D) histological techniques have provided reliable insight into cellular morphology and spatial organization, but they are limited to thin planar sections (<50 μm), offering only isolated snapshots of complex three-dimensional (3D) tissue architecture. Similarly, techniques such as RNA sequencing and spatial transcriptomics offer important gene expression data, but lack the spatial resolution needed to resolve fine-scale cellular organization across whole organs. This is particularly limiting in the lung, where the branching airway and alveolar architecture span the entire organ, demanding more volumetric analysis to preserve physiological context.

Imaging

To achieve higher spatial and volumetric images of intact tissues, medical imaging tools such as optical coherence tomography (OCT) — employed by our lab to image lung architecture at high depths — magnetic resonance imaging (MRI), computed tomography (CT), and positron emission tomography (PET) enable visualization of

larger-scale structural features across the organ, but are limited in their ability to capture cellular-scale biological detail or label distinct cellular or molecular information. Fluorescence microscopy fills this gap by imaging distinct, fluorescently labeled structural, cellular, molecular, and genetic targets with high spatial resolution. However, imaging depth of optical microscopy is limited in thick tissue sections, especially in the lung due to high light scattering at the alveolar-air interfaces. For example, imaging through intravital windows and ex-vivo Crystal Ribcage — a transparent housing engineered by our lab for multiscale imaging of the intact murine lung — have enabled impressive visualization of dynamic processes on the lung surface while critically preserving live lung function [1–3]. However, these methods remain constrained by limited imaging depth, failing to capture internal 3D architecture beyond superficial alveolar layers (less than one air-filled alveolus).

Multiplexing with fluorescence microscopy

Another benefit of fluorescence microscopy is compatibility with the emerging development of immunofluorescent multiplexing. This technology enables simultaneous visualization of multiple molecular targets within the same tissue section by cyclically, fluorescently labeling the sample, imaging, then removing or bleaching the old fluorophores to allow for another panel of targets to be labeled and imaged [4]. Techniques such as cyclic immunofluorescence (cyCIF), iterative bleaching and staining (IBEX), and iterative indirect immunofluorescence imaging (4i) have captured tens of markers at a time within thin cell or tissue sections [5–10]. These platforms, however, are largely confined to thin samples due to challenges in antibody diffusion, optical access,

and signal preservation in thick tissues. Expanding multiplexing to volumetric tissue imaging remains an open area of development.

Clearing

Two general approaches have been explored for resolving the full 3D molecular architecture of tissues via optical microscopy: (1) reconstruction of serial histological sections and (2) optical clearing and whole-organ imaging. The former, exemplified by techniques such as CODA [11], retains the histological advantages of thin section immunolabeling and compatibility with clinical samples. However, sectioning imposes inherent challenges in registration and tissue loss across thousands of slices. Conversely, clearing-based methods (e.g., DISCO, CLARITY, CUBIC) [12–14] have been designed to allow for imaging whole, intact organs: By rendering fixed tissues optically clear via chemical index of refraction matching and dissolving non-target tissues, imaging depths can be increased to span entire organs while preserving 3D tissue geometry. These protocols have been largely optimized for the brain — the pioneering organ — to study things like brain-wide connectivity and function, although it has seen success with the lung and other organs. Recent studies have in whole cleared murine lungs have demonstrated large airway mapping, fibrosis, nano-particle aerosol distribution, and lymphatics [15–19]. However no studies to date have imaged alveolar to cellular resolution on an organ-wide scale, nor highly multiplexed fluorescent staining (more than 2 to 4 markers at a time). In part, this is due to the large size of whole cleared organs creating slow immunolabel diffusion as well as some fluorophore quenching in different

clearing solvents. Therefore, achieving more resolved and multiplexed volumetric imaging of lungs is desirable.

Bridge clearing and multiplexing

Given these challenges, there is growing interest in hybrid strategies that combine sectioning and other strategies with modern multiplexing protocols to interrogate large tissue volumes. Recently Park and Chung et al. have achieved highly multiplexed imaging of the human brain with an integrated platform for slicing, clearing, and labeling [10]. Effectively, slicing the organ into manageable sections allows for rapid and uniform immunolabeling staining and subsequently faster rounds of multiplexing. Our goal is to adapt these principles to the murine lung — developing a robust, reproducible pipeline that integrates tissue sectioning, high-resolution confocal imaging, optical clearing, and multiplex fluorescence labeling, ultimately enabling 3D reconstruction of structural, cellular, and molecular information across the lung. Termed the Functional Lung Atlas, novel goals include organ-wide alveolar to cellular resolution, as well as complete mapping of cell types, airways, and mechanical functions in the lung. Specialized in our lab, functions include static deformation mapping [20], and airway and vascular flow. These are visualized in figure 1.

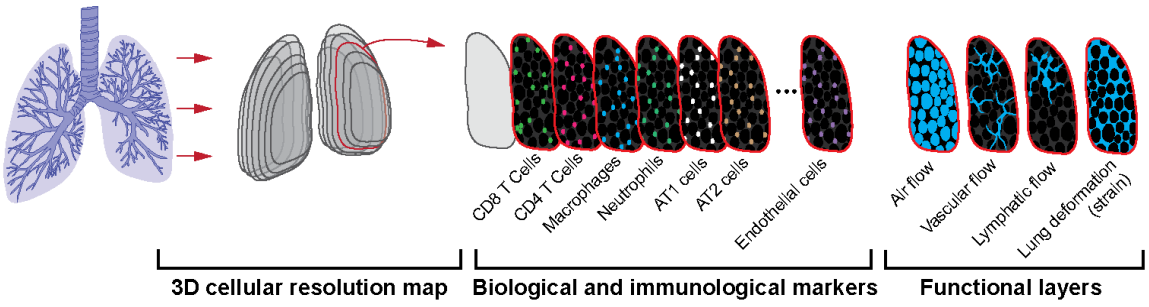

Figure 1. Schematic representation of Functional Lung Atlas components

Aims

This thesis is broken into 2 specific aims focused on establishing protocols for preparing and imaging lung slices as well as creating an example visualization of smaller volume regions of interest demonstrating resolution, image alignment, and example features desired for the final lung atlas.

Aim 1: Create and optimize initial protocols for lung sample slicing, optical clearing, imaging, and slice housing/mounting. This aim was accomplished by testing agarose filling and embedding of lung samples for slicing via compresstome and vibratome. Optical tissue clearing was tested using 2,2-thiodiethanol (TDE), comparing imaging depth resolutions achieved by a range of %TDE solutions in PBS. Imaging was done with fluorescent confocal microscopy, comparing between various objective magnifications and three different microscopes to optimize for pixel resolution in three dimensions and image acquisition speed. Finally, slice mounting was optimized by testing different microscope slides, cover glass, well plate, and agarose embedding to flatten the slice for imaging while limiting compression or distortion.

Aim 2: Align images to create example visualization at desired resolution and with some fluorescently stained features. Smaller volume regions of interest (ROI's) from full slices were imaged at high resolution and aligned to effectively create the example visualizations while avoiding large data and alignment computation. Sequential slice images were computationally aligned or registered using image processing toolboxes in ImageJ and MATLAB, primarily manual control point selection between adjacent slices. We found that aligning confocal images by themselves resulted in slightly incomplete

and distorted volumes, so sequentially sliced and overlapping slice images were taken on an OCT-vibratome, section tomography system to create a complete structural scan of the lung before staining slices for confocal imaging. Fluorescent confocal images of the same slices were then aligned to the intact structural scan to produce a volume more representative of the lung's original geometry. Finally, example features such as DAPI stained nuclei, endogenous labeled tdTomato structure and EGFP neutrophils, and DiD delivered via aerosol were imaged.

AIM 1: PROCEDURE OPTIMIZATION

Introduction

To enable volumetric imaging of the murine lung with high structural and molecular resolution, it was necessary to first establish protocols for sample preparation, clearing, and imaging optimized for thick tissue slices. While whole organ clearing techniques can achieve deep optical penetration, they often result in slow immunolabel diffusion, potential structural distortion, and fluorescence quenching, particularly in fragile tissues like the lung. As a result, this project focused on a hybrid approach of tissue slicing combined with optical clearing to balance imaging depth, tissue preservation, and future compatibility with multiplex immunolabeling strategies. Slicing the lung into sections reduces diffusion barriers for antibodies and fluorescent dyes, facilitating rapid and uniform labeling across the sample volume — an important consideration for future multiplexed imaging workflows. Available imaging modalities at Boston University's Micro and Nano Imaging Facility and Neurophotonics Center, including the Olympus FV3000 laser scanning confocal, the Nikon W1 spinning disk confocal, and a custom Nikon CSU-X1 upright spinning disk confocal microscope in our lab, were compared to optimize imaging resolution and speed. Although other modalities such as two-photon and light sheet microscopy can offer advantages in imaging depth, their limited accessibility within the lab directed efforts toward confocal-based approaches for this study.

For tissue clearing, a simple refractive index (RI) matching strategy using 2,2'-thiodiethanol (TDE) (Fig. 2) was selected over more aggressive organic solvent-based

methods such as 3DISCO, which in prior experiments caused tissue hardening and fluorescence degradation. TDE offers a simple procedure, minimal tissue perturbation, full miscibility in water, and tunable RI matching by adjusting concentration, thus providing flexibility to optimize clearing for our specific samples [21–24].

In total, optimizing lung inflation and slicing, clearing with TDE, microscopy and imaging, and slice mounting laid the groundwork for achieving high-content, volumetric images of the lung suitable for later multiplex labeling, 3D reconstruction, and functional analysis.

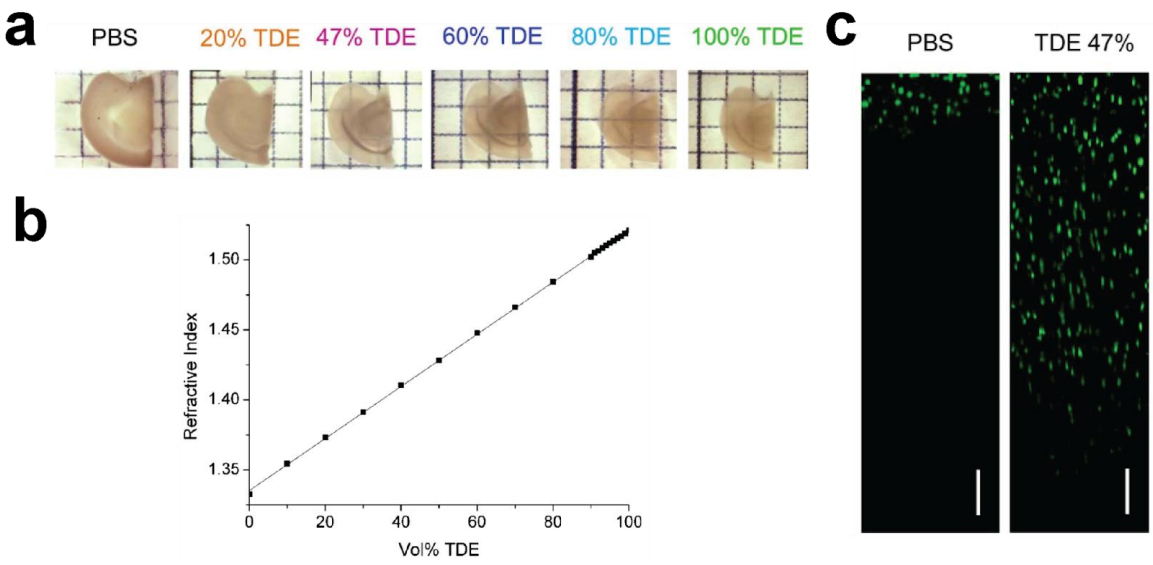

Figure 2: From[22] (a) murine brain slabs cleared and immersed in varying percentages of TDE in solution with PBS. (b) RI matching can be controlled via TDE concentration. (c) labeling depth of DAPI by 2-photon microscopy

Materials and Methods

Mice

All animal procedures were conducted in accordance with protocols approved by the Boston University Institutional Animal Care and Use Committee (IACUC) and

adhered to established ethical guidelines. Mice were housed and bred under pathogen-free ambient temperature, humidity and light–dark conditions at the Boston University Animal Science Center. Experimental animals were primarily derived from a colony of transgenic B6.129(Cg)-Gt(ROSA)26Sortm4(ACTB-tdTomato,-EGFP)Luo/J mice (referred to as mTmG; Jackson Laboratory, stock no. 007676), which ubiquitously expressed membrane-localized tdTomato fluorescence, enabling visualization of overall tissue architecture. Additionally, one mouse expressing EGFP labeled neutrophils was used, derived from a colony where Male B6.Cg-Tg(S100A8-cre,-EGFP)1Ilw/J mice (MRP8-Cre; Jackson Laboratory, stock no. 021614), which express Cre recombinase under the S100A8 promoter specific to neutrophils, were crossed with homozygous mTmG females to generate MRP8-mTmG reporter mice. All mice used in experiments were of C57BL/6 background and ranged in age from 6 to 12 weeks old.

Slicing

To support airway structure during slicing, mouse lungs were first inflated with 2% low-melting-point agarose (Sigma-Aldrich) dissolved in phosphate-buffered saline (PBS). PBS was used to maintain tissue swelling stability and pH during and after preparation. The agarose solution was maintained at 40°C to ensure it remained liquid during the filling process. Following inflation, lungs were fixed by immersion in 10% neutral-buffered formalin (Thermo Fisher Scientific) in a 20 mL glass vial at room temperature for approximately 12 hours, after which they were washed with 1x PBS three times. Fixed samples were then embedded in 2% agarose within a stainless-steel specimen tube designed for the vibrating microtome (Compresstome model F00395A,

Precisionary Instruments LLC). Samples were sectioned at thicknesses ranging from 10 µm to 1000 µm using the compresstome. The resulting slices were carefully collected from the surrounding PBS bath using a spoon or tweezers and transferred to 24-well plates containing PBS to keep the slices hydrated. In cases where fixation was not performed on whole lungs prior to slicing, individual slices could be post-fixed after sectioning.

Microscope and imaging optimization

To optimize volumetric imaging of lung tissue sections, z-stacks were acquired to capture three-dimensional structural information, with orthogonal reslicing along the YZ or XZ planes performed in ImageJ to validate z-resolution. Tissue structure was visualized by imaging membrane-localized tdTomato fluorescence expressed by mTmG mice, using a 561 nm excitation laser.. Multiple microscopes and objectives were compared to assess differences in cross-sectional x-y-resolution (XY plane) and axial z-resolution (YZ or XZ planes), as well as imaging speed across tiled regions of interest. Imaging was conducted with appropriate Nyquist-sampled z-steps according to each objective's numerical aperture (NA) and optical resolution.

Three microscopes were evaluated: An Olympus FV3000 laser scanning confocal microscope with objectives including 10x (UPLSAPO10X2, 0.4 NA, 3 mm working distance [WD], 4.14 µm z-step), 20x (UPLSAPO20X, 0.75 NA, 0.6 mm WD, 3.24µm z-step), 20x (LUCPLFLN20X, 0.45 NA, extended 6.6–7.8 mm WD, 3.24µm z-step), and 40x (UPLSAPO40X, 0.9 NA, 0.11–0.23 mm WD, 0.62µm z-step); A Nikon W1 SoRa spinning disk confocal microscope with objectives including 10x (PLAN APO λD, 0.45

NA, 4 mm WD, 2.5µm z-step), 20x (S PLAN FLUOR LWD 20×C, 0.7 NA, 2.3 mm WD, 1µm z-step), and 40x (0.6µm z-step)immersion objective; and a Nikon CSU-X1 upright spinning disk confocal microscope with objectives including 10x (2.5µm z-step), and 20x (0.8µm z step).

Performance was evaluated based on two factors: (1) Visual assessment of x-y and z-resolution in resliced images, with the goal being to distinguish alveolar to cellular structures and (2) An estimation of imaging speed or throughput, particularly for large tissue volumes requiring tiled multi-region acquisitions. Imaging time for each microscope objective was roughly calculated by imaging a whole slice, considering image tilling required to encompass odd slice shapes, then multiplying that time across a whole lung volume, roughly approximated as $1cm^3$. It is important to note that this is a very rough estimate as the time will vary largely depending on different tissue size, shape, and image stitching requirements. Therefore, the calculation is better used as a measure of microscope comparison rather than accurate timing, which may require imaging the full volume to accurately measure. The optimal microscope and objective combinations were selected based on achieving sufficient resolution at reasonable imaging speeds suitable for large-volume, high-content 3D reconstructions.

Tissue clearing

The optimal concentration of 2,2'-Thiodiethanol (TDE; ≥99%, cat. no. 111-48-8, Sigma-Aldrich) for clearing agarose-filled lung tissue was determined by comparing imaging performance across a range of TDE concentrations: 0% (negative control), 20%, 40%, 60%, 80%, and 100%. Based on published protocols and prior work by Nia Lab

member Kathryn Regan, Ph.D., the following procedure was employed: lung tissue was first sliced into 1 mm thick sections using the previously described slicing method and stored in 1× PBS until clearing. TDE solutions of varying concentrations were prepared by diluting 100% TDE stock with 1× PBS. For clearing, tissue slices were immersed in TDE solutions within well plates, and to minimize tissue shrinkage, serial incubations with gradually increasing TDE concentrations were performed. Samples were incubated for one hour at each concentration at 37 °C with mild agitation until reaching the target clearing concentration. For example, slices cleared to 60% TDE underwent sequential one-hour incubations in 20%, 40%, and finally 60% TDE solutions. Cleared slices were then imaged using the Olympus FV3000 confocal microscope while submerged in TDE. Volumetric z-stacks were acquired, imaging the tdTomato-labeled tissue structures. Image quality and clearing efficacy were visually assessed signal intensity and imaging depth in both the XY and YZ planes.

Slice housing and image mounting

Traditional mounting methods, such as placing lung slices on a glass microscope slide or immersing them in a liquid-filled well, often resulted in samples being out of plane relative to the imaging axis, leading to uneven focus across large surfaces. To address this distortion and reduce the need for post-processing corrections, custom physical mounting devices were developed with the goals of flattening both sides of the slice while avoiding compression, preserving optical clarity from TDE clearing, and maintaining sample hydration.

Initial mounting strategies (Fig. 3) were tested but failed to meet all criteria. These included: floating the lung slice in a TDE-filled well approximately 1 mm deep (Fig. 3a); mounting the slice on a glass slide with a drop of TDE and covering with a cover glass (Fig. 3b); adhering the slice to a glass slide using Cell-Tak (Corning, cat. no. 354241, 1–5 µg/cm²) (Fig. 3c); embedding the slice in a 2% agarose–TDE mixture (Fig. 3d); and drying the slice directly onto a glass surface such as a well plate bottom (Fig. 3e). Common issues included incomplete flattening, loss of refractive index (RI) matching due to insufficient TDE immersion, and dehydration of the tissue.

The most successful design involved sandwiching the lung slice between two glass coverslips with a spacer matching the sample thickness to provide structural support. In the first prototype (Fig. 4a), a polydimethylsiloxane (PDMS; Sigma-Aldrich, 1:10 base to curing agent ratio) spacer was fabricated by molding and cutting wells to match the slice dimensions, followed by plasma bonding the spacer to a glass coverslip. The well was filled with TDE, the slice was placed inside, and a second coverslip was gently placed on top, held in position by fluid surface tension. To further improve structural stability, a second design iteration (Fig. 4b) incorporated an acrylic sheet bonded to the coverslip with epoxy adhesive (FH-5315, Epolite) and a plastic shim (McMaster-Carr) for precise height control. Finally a 3D resin-printed microscope slide (FormLabs Form 3, Clear Resin V5) was designed for easier and more reproducible fabrication while maintaining stability and precision of the acrylic-shim design (Fig. 4c,d). Flattening was tested by imaging whole slice planes while slice compression due to the cover glass was assessed with top-to-bottom images of slices and checking the width of the cross-sectional images.

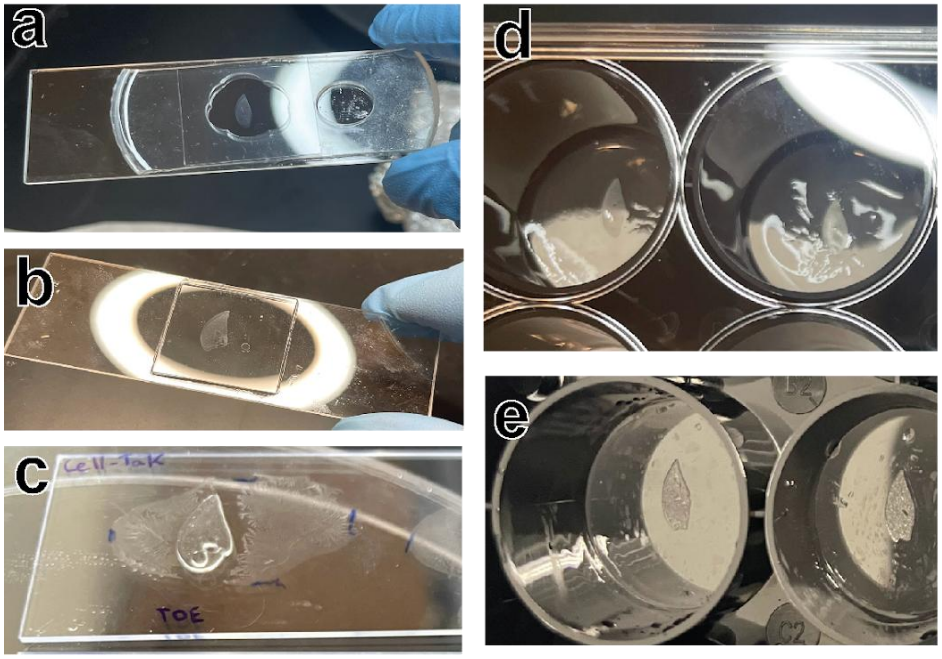

Figure 3: Slice mounting methods that failed. (a) slice floating in TDE filled well –roughly 1 mm deep. (b) slice on glass microscope slide with drop of TDE and cover glass on top. (c) Slice adhered to glass microscope slide via Cell-Track. (d) slide embedded in 2% agarose and TDE. (e) Slide dried onto glass (well plate glass bottom)

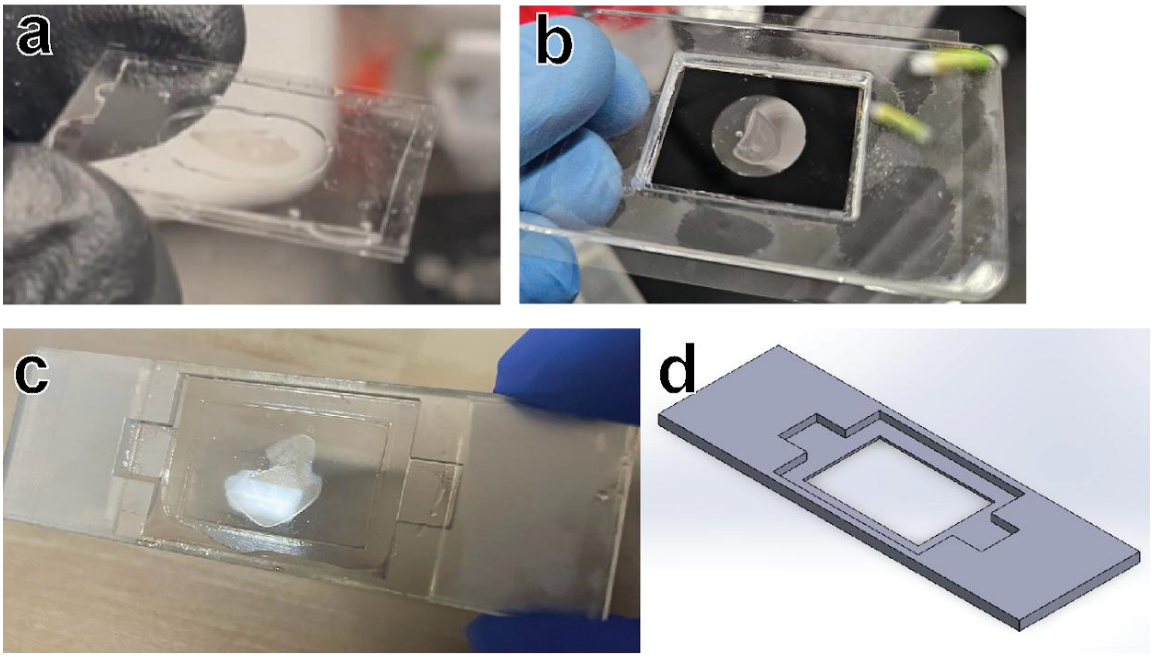

Figure 4: Spacer with cover glass prototypes. (a) PDMS spacer with cover glass faces. (b) plastic shim spacer on top of cover glass, placed in acrylic well and sealed with ecoflex. (c)(d) 3D resin printed microscope slide with cover glass faces

Results

Microscope resolution and imaging speed comparison

Cross-sectional (XY) and axial (YZ) images of lung slices acquired using the Olympus FV3000 (Fig. 5a), Nikon W1 spinning disk (Fig. 5b), and Nikon X1 microscopes (Fig. 5c) were compared across multiple objectives to assess image resolution and volumetric imaging capability. Clear distinction of tdTomato-labeled alveolar structure from airway spaces was considered the minimum acceptable resolution, with visible cellular features considered advantageous. As expected, objectives with higher numerical apertures and pixel resolution produced superior image clarity. In the native XY view, alveolar walls were distinctly resolved for all objectives at magnifications of 10x and above. However, axial resolution in the YZ plane was consistently lower across all systems, establishing z-resolution as the limiting and therefore defining factor.

At 10x magnification, z-resolution appeared somewhat blurred, but some objectives such as the W1 10x and Olympus 10x at maximal resolution remained acceptable for structural analysis. Imaging with 20x and 40x objectives provided significantly improved axial resolution and clearer cellular features. Lower magnifications such as 4x did not yield meaningful z-resolution and were excluded from further analysis. Imaging speed was estimated and plotted against qualitative z-resolution scores (Fig. 6). While Olympus, W1, and X1 systems at 10x and 20x offered reasonable imaging times, higher magnifications and SoRa zoom settings dramatically increased acquisition times. Although resonant scanning on the Olympus FV3000 decreased scan

time, it substantially degraded image quality. Overall, the W1 and X1 spinning disk systems demonstrated the best balance between speed and resolution, with 10x objectives favoring faster acquisition and 20x objectives providing improved z-resolution at moderate imaging times.

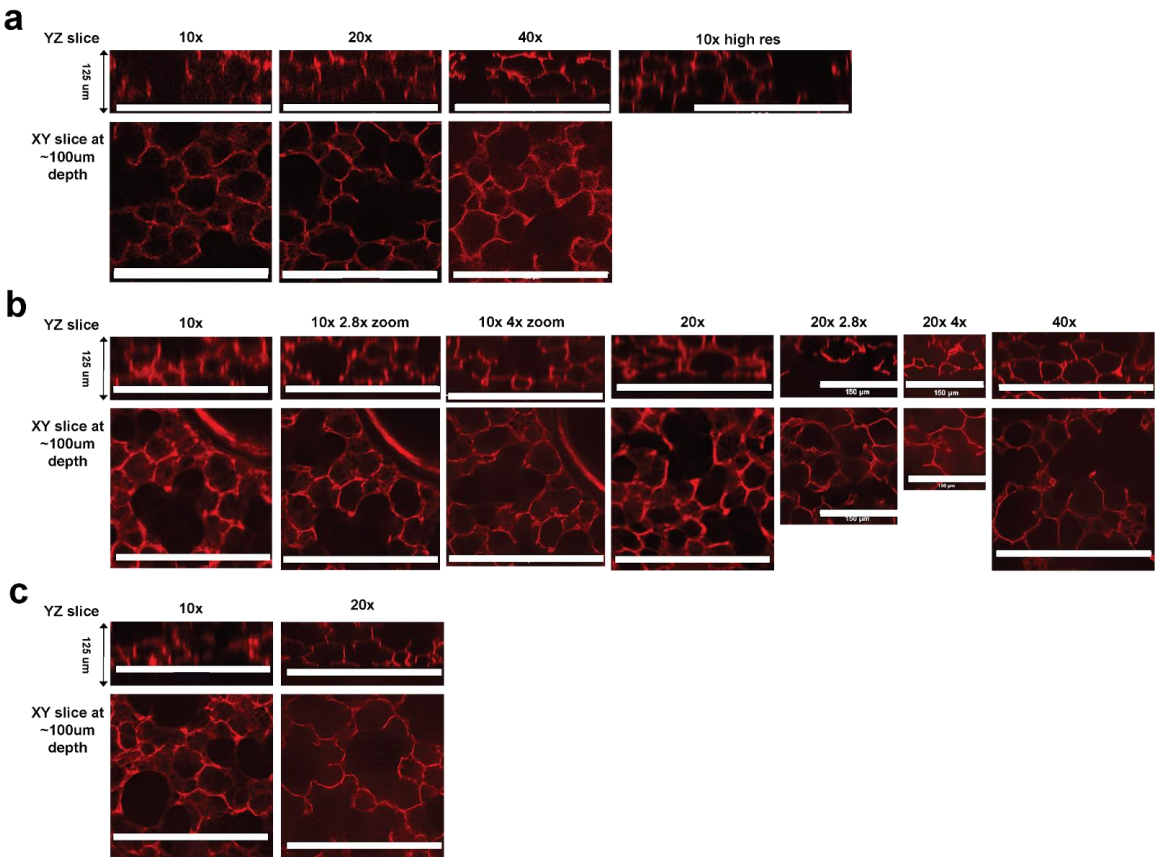

Figure 5: Microscope resolution comparison. Scale Bars at 300 µm unless labeled 150 µm. (a) Olympus. (b) W1 objectives and SoRa zooms. (c) X1 objectives

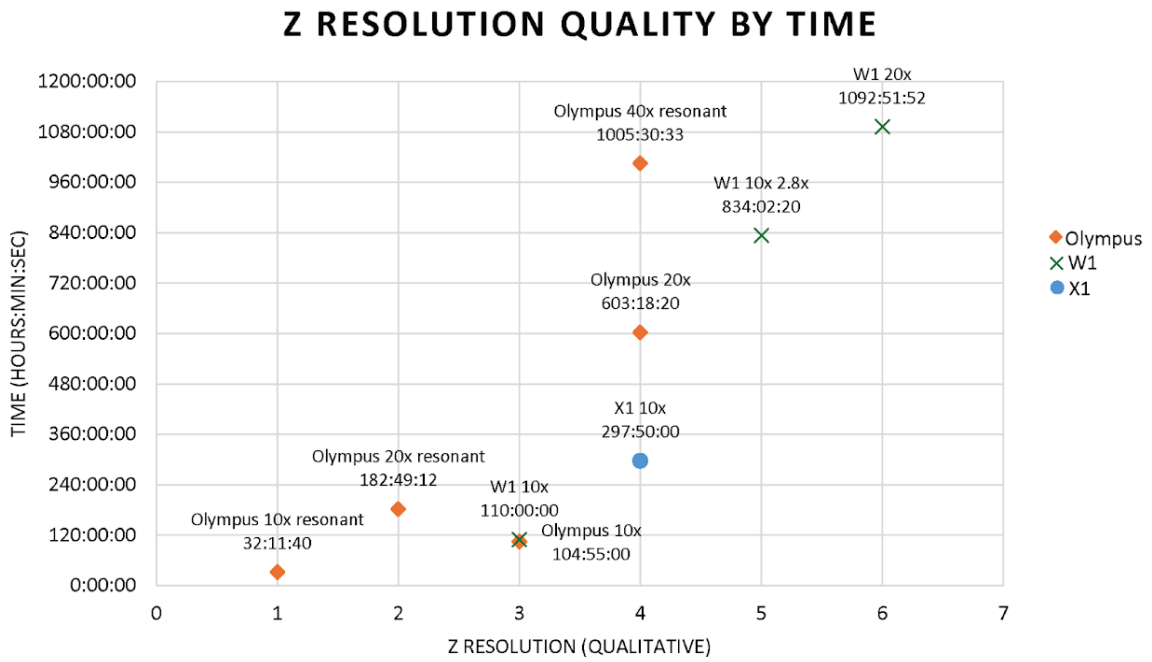

Figure 6: Microscope imaging time estimations across qualitative Z-resolution scores. Objectives that had significantly higher imaging times were cropped out

Tissue clearing

Lung slices were imaged at 10x magnification using the Olympus FV3000 following clearing with varying concentrations of TDE (Fig. 7). Increased TDE concentration correlated with improved imaging depth and signal clarity. Slices cleared with lower TDE percentages (0–40%) exhibited significant signal attenuation and blurring beyond about 150–200 µm depth. In contrast, samples cleared with 80% and 100% TDE maintained image signal intensity and structural clarity up to 300–400 µm depth. Based on these findings, 80% TDE was determined to provide the optimal balance of tissue transparency and imaging depth for agarose-filled, fixed lung slices.

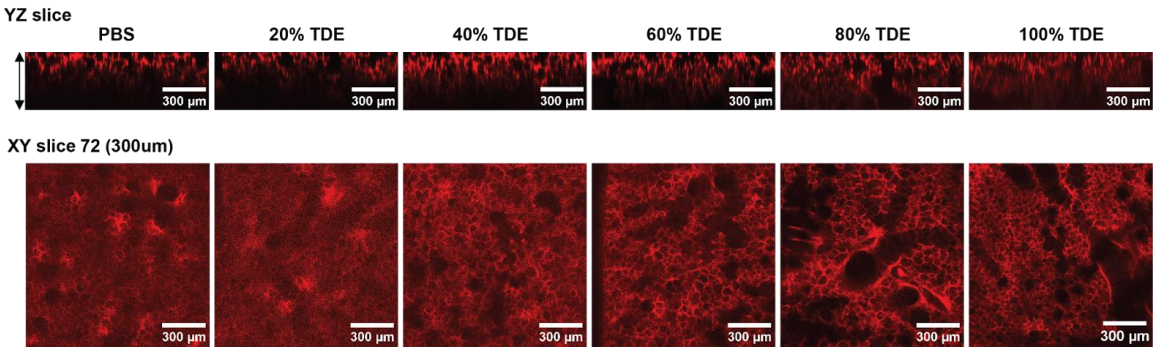

Figure 7: Image depth comparison between TDE% in clearing solution. 80% TDE results in best image depth resolution

Slice flattening and compression validation

Comparisons of slice mounting methods demonstrated that sandwiching the lung slices between two glass coverslips using custom-fabricated spacers resulted in significantly improved surface flatness compared to traditional mounting methods (Fig. 8). Tracing the top and bottom edges of the slices in cross-sectional images confirmed that flattening occurred without visible tissue compression. The sandwich mounting technique allowed TDE immersion and refractive index matching during imaging, while preserving tissue thickness, flattening the slice, and additionally allied for imaging on both sides of the slice through either cover glass.

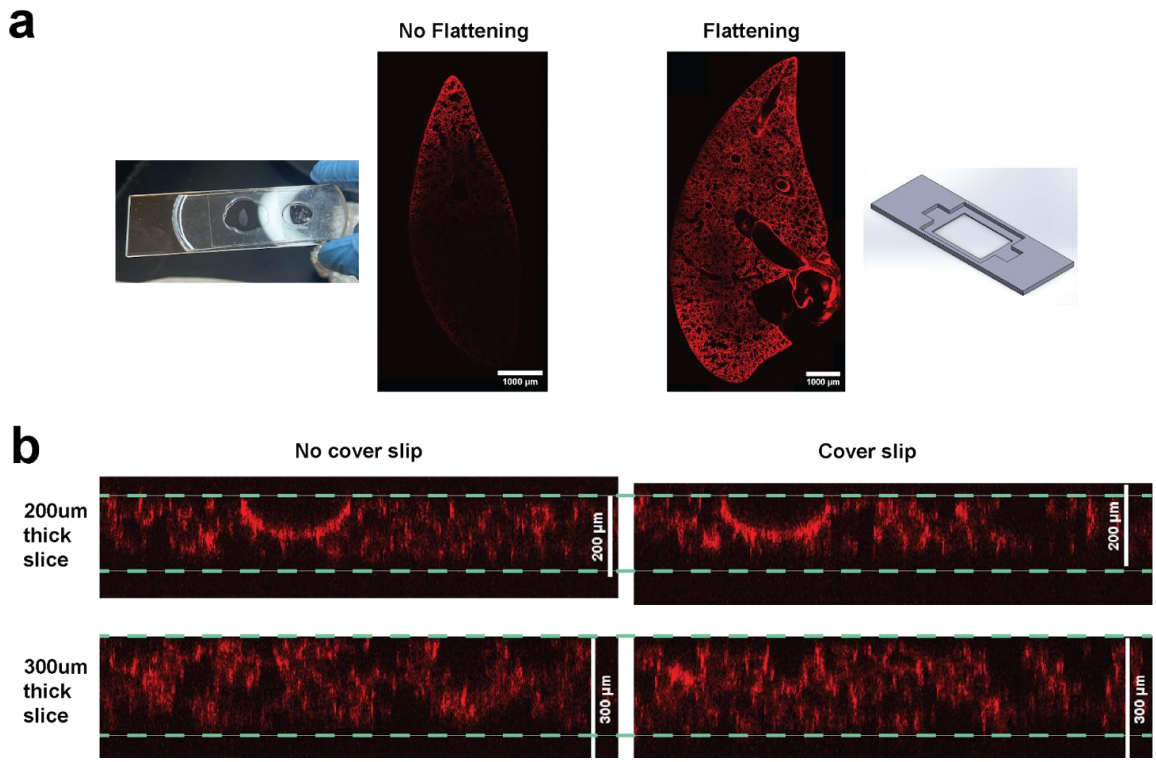

Figure 8: (a) Slice flattening. (b) cover glass sandwich compression validation

Discussion

The W1 spinning disk confocal microscope equipped with 10x and 20x objectives provided the optimal combination of imaging speed and resolution for large-volume lung imaging. This outcome is consistent with the known advantage of spinning disk systems providing faster image acquisition times compared to slower point-scanning confocal systems. Objectives with low working distances or requiring immersion were deemed impractical for deep z-stack imaging of thick slices due to limited working depth. Alternative imaging modalities such as two-photon microscopy or light sheet microscopy may offer improved imaging depth, speed, or axial resolution. These were not evaluated in the current study and could provide future imaging optimization. Furthermore,

improvements in tissue prep or microscopy techniques could further reduce image acquisition times and increase resolution.

For tissue clearing, 80% TDE was identified as the optimal clearing solution for agarose filled, fixed lung slices, providing maximal imaging depth without significant structural deformation. Although more quantitative measurements such as refractive index matching or light transmittance were not performed, image resolution was the final desired result and provided direct visualization of signal preservation at depth. Additionally, nuances in the TDE clearing procedure were noted that may need further testing — tissue stability or clearing quality reducing over time in TDE, perhaps due to things like particulate formation when refrigerated.

The sandwiching slice mounting method developed — using glass coverslips and spacers to maintain sample thickness and immersion in TDE — successfully flattened slices for large area imaging while preserving tissue integrity. However, limitations remain such as slice movement and distortion as well as bubble formation while applying the top cover glass. Future iterations could improve on ease of use, limiting tissue distortion, and upscaling size to house multiple slices in parallel, enabling high-throughput imaging workflows.

AIM 2: SLICE ALIGNMENT AND EXAMPLE VISUALIZATION

Introduction

Using the initial protocols for lung tissue slicing, clearing, and imaging established in Aim 1, the next objective (Aim 2) was to demonstrate aligned volumetric reconstruction of lung sections, incorporating fluorescently labeled cellular and structural features. Specifically, this aim focused on creating smaller volume examples at high resolution to validate the feasibility of future organ-scale mapping.

Traditional serial sectioning approaches often introduce tissue loss and deformation from slicing, complicating image reconstruction. While directly aligning confocal images of adjacent slices can provide 3D volumes, distortions and tissue loss between sections limit continuity of the volume. To address this, we implemented a sequential slicing strategy combined with optical coherence tomography (OCT) imaging to create an intact structural reference volume. For background, sequential slicing or section tomography is a well-established method for acquiring tomographic images of biological samples [25–28]. By cyclically imaging the sample surface then slicing, overlapping images can be obtained. Confocal fluorescence images of slices were then registered to this OCT-derived scaffold, correcting for deformation and enabling a more anatomically accurate reconstruction.

This chapter details the alignment strategy, integration of OCT structural imaging, feature-specific fluorescent imaging, and outlines the initial demonstrations of volumetric fluorescent mapping toward a functional lung atlas.

Materials and Methods

Alignment

Initial attempts at computational alignment were conducted using established translational, rigid, affine, and non-linear transformations applied to whole-slice and smaller ROI datasets in MATLAB (Image Processing Toolbox) and ImageJ (BigStitcher and BigWarp plugins, [29]). Automatic methods proved unreliable due to slice deformation and limited landmark consistency. Therefore, manual control-point registration was used: corresponding anatomical landmarks (e.g., vascular or airway bifurcations) were manually selected in adjacent slice images to guide alignment and generate transformation matrices.

Fluorescent confocal image stacks were pre-processed to optimize contrast, and alignment transformations were iteratively refined to minimize poorly registered regions. Final aligned stacks were visualized using 3D volume rendering tools in ImageJ [29] and MATLAB.

Sequential slicing and OCT imaging

To overcome tissue loss and distortion between physical slices, we implemented a sequential slicing and imaging strategy using OCT. OCT provides high depth penetration — multiple millimeters in depending on clarity — allowing for deep, non-destructive imaging of intact structures between slices. Sequential imaging and slicing generated overlapping volumetric images, enabling gapless alignment. Sequential imaging was performed on two OCT systems: (1) A custom section tomography with PS-OCT and 2P

system custom made and generously lent by Dr. Boas's lab (Fig. 9b) [30, 31]; and (2) A commercial Thorlabs Telesto OCT system for higher resolution imaging of structural detail (Fig. 9c).

Using the section tomography, PS-OCT system, slices were immersed in a PBS bath, and cut at ~450 μm thickness, imaged a bit deeper, and then sectioned again. With the integrated 4x air objective (Olympus, UPLFLN4x, NA 0.13) a 3x3x3.5 μm^3 voxel size was achieved. Alternatively, using the commercial OCT system compatible with 10x objective, 3×3×2.59 μm^3 voxel size was achieved. With the commercial OCT, the sample had to be sliced at the custom system, then manually moved to the OCT for imaging. This was a tedious procedure not optimized for large volume imaging, but it was efficient for getting an example volume to demonstrate feasibility of this approach. Incorporating TDE clearing, images could be taken deeper than 600 μm. The resulting slices from the OCT serial sectioning were then imaged on the confocal images of fluorescently stained slices were then registered to the OCT volume to correct for structural distortions arising during slicing and sample handling.

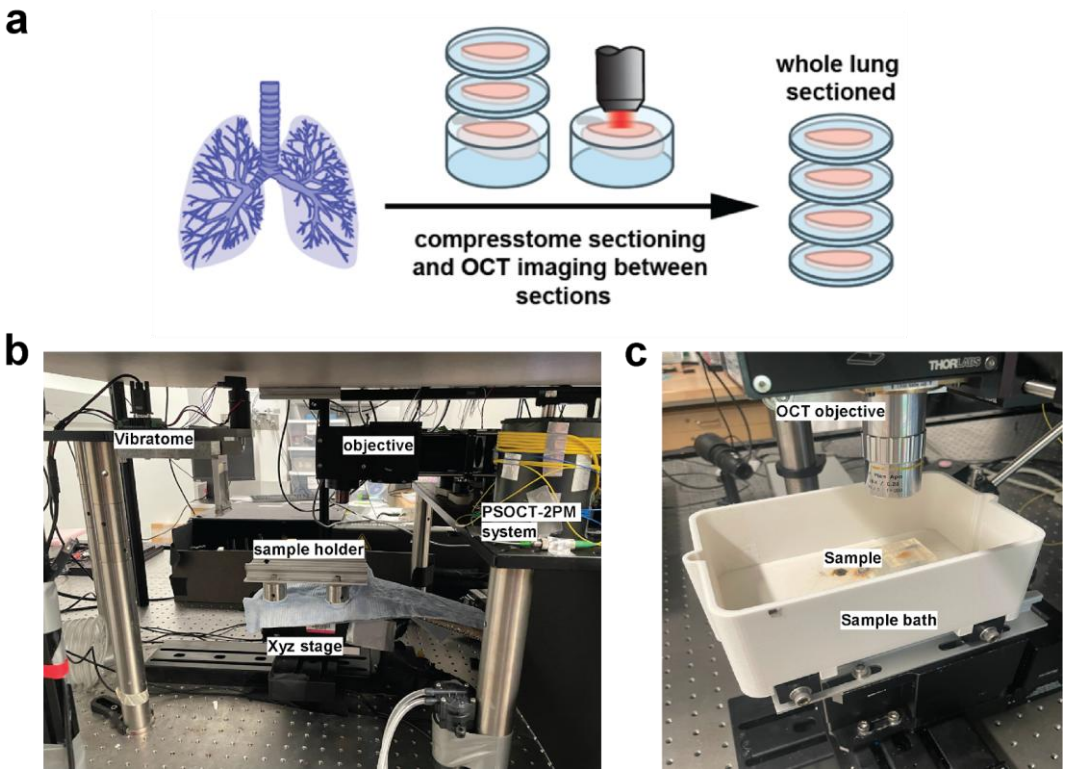

Figure 9: Sequential slicing and OCT imaging. (a) Schematic graphic of sequential slicing and OCT imaging. (b) labeled diagram of Boas lab's custom section tomography PS-OCT system. (c) labeled diagram of sample being imaged by commercial OCT with 10x objective

Fluorescent feature demonstration

To test volumetric, fluorescent feature visualization, and see how clearing effects their fluorescence, four fluorescent markers were selected. Structural architecture was labeled by endogenous membrane tdTomato fluorescence (mTmG reporter mice). Nuclei were labeled by Hoechst 33342 (Sigma, 10mg/ml, 1:1,000 dilution) and DAPI staining (Thermo Fisher Scientific, 62248, 5mg/mL, 1:5,000 dilution) to show individual cells. As an example of immune cells, neutrophils were labeled by endogenous EGFP-expressing expression (MRP8-mTmG mice). DiD aerosol delivery (Thermo Fisher Scientific) through the trachea into the lung airways was used to visualize inhaled particle distribution — a process being studied by Gabrielle Grifno in our lab.

Fluorescent images were acquired using the Nikon W1 at 20x magnification, optimizing for ~0.33 µm x 0.33 µm x 1 µm voxel resolution. For nuclear staining optimization, both Hoechst 33342 and DAPI dyes were compared before and after TDE clearing: 1 mm^3 samples were stained before, after, or during TDE clearing, then mounted in PBS or TDE for imaging, with a no stain control.

Results

Alignment

Three consecutive fluorescent confocal slices were successfully aligned into a three-dimensional volume using manual control point registration (Fig. 10). When observing the XZ view (Fig. 10a) and adjacent slice faces (Fig. 10b), a discontinuity of structure can be seen. This suggests a small amount of tissue was lost when slicing. Structural distortions, including warping and localized collapse of alveolar walls, were also visible across adjacent slices. These findings emphasized the necessity of incorporating an initial, intact structural image to guide full-volume reconstruction.

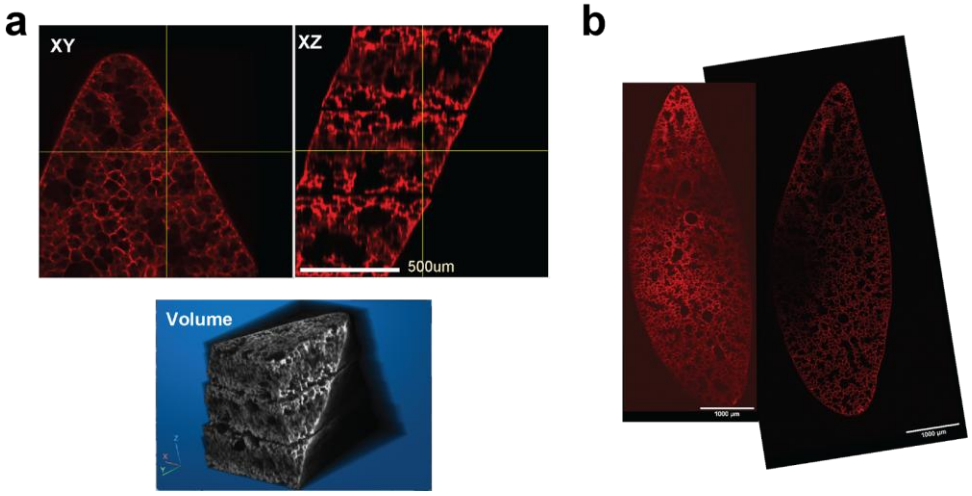

Figure 10: Confocal image slices aligned. (a) XY, XZ, and volume visualization of three aligned slices. (b) example of two adjacent slice faces at a slice boundary

Sequential slicing and OCT imaging

Sequential OCT imaging of sliced lung tissue demonstrated effective overlap and continuity between adjacent sections (Figs. 11, 12). The custom PS-OCT system at 4x magnification lacked the resolution needed to resolve alveolar structures (Fig. 11). In contrast, imaging with the commercial Thorlabs Telesto OCT system at 10x successfully captured alveolar morphology with sufficient resolution in both axial and planar views. Subsequent registration of confocal fluorescence images to the OCT-derived structural image corrected visible slice distortions (see XY views) and produced a less distorted 3D lung volume (Fig. 13).

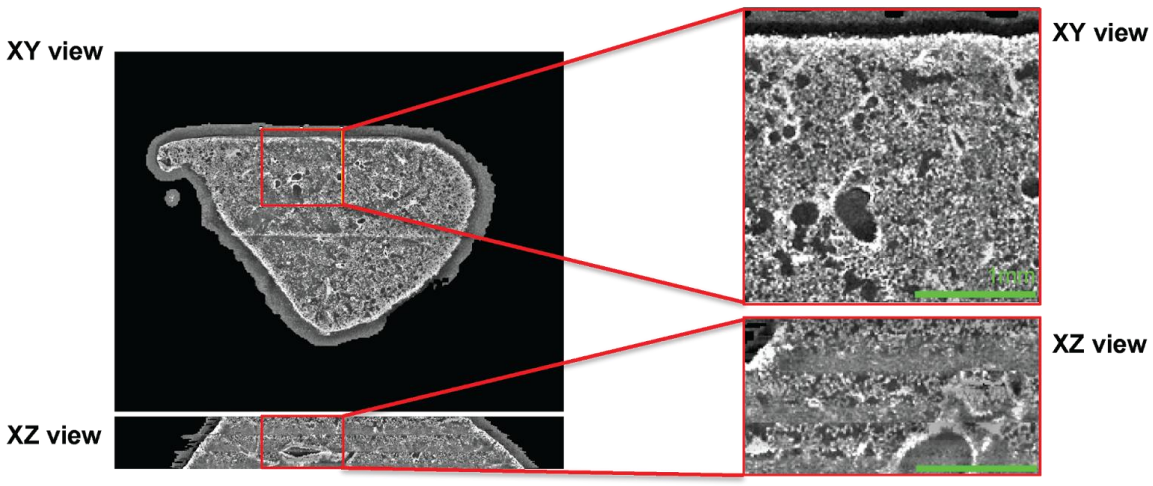

Figure 11: Sequential slicing and imaging using custom PS-OCT system. Low-resolution OCT imaging across sequential slices captured gross structural continuity but lacked sufficient resolution to resolve alveolar architecture.

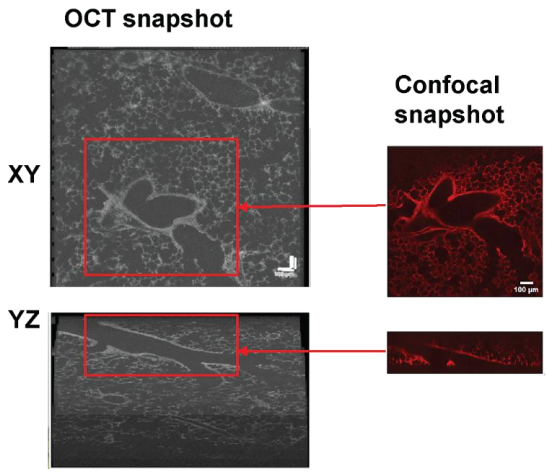

Figure 12: Sequential slicing and imaging using commercial Thorlabs OCT system. Higher-resolution OCT imaging enabled visualization of alveolar structures and maintained overlap between sequentially sliced sections.

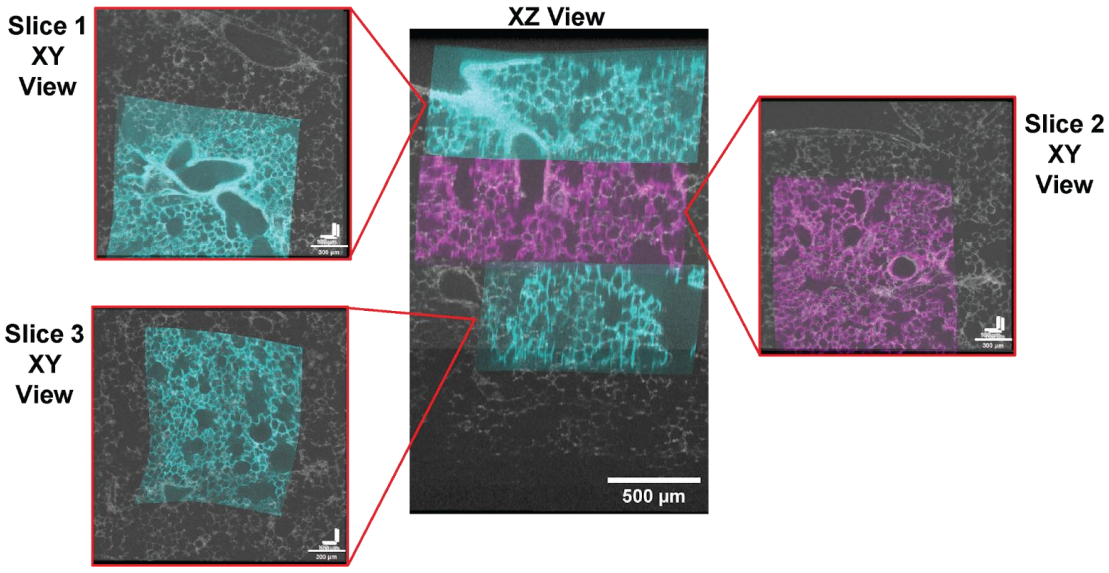

Figure 13: *Registration of confocal fluorescence images to OCT-derived structural scaffold.* Confocal slices (20x objective) were individually deformed relative to the OCT volume; registration corrected distortions and restored anatomical continuity.

Fluorescent feature demonstration

In examining nuclear labeling strategies, Hoechst 33342 fluorescence was found to be significantly quenched (matching background fluorescence of control rather than distinct nuclei) following TDE clearing (Fig. 14a), whereas DAPI staining remained robust and consistent (Fig. 14b). DAPI was thus selected as the preferred nuclear marker

for subsequent experiments. Composite imaging, overlaying DAPI-labeled nuclei, EGFP-positive neutrophils, and tdTomato-labeled structural membranes revealed distinct cellular and structural features within the same reconstructed volume (Fig. 15). While high lateral (XY) resolution was maintained, axial (Z) resolution remained comparatively lower, showing the need for future optimization of clearing and imaging parameters to enhance volumetric resolution.

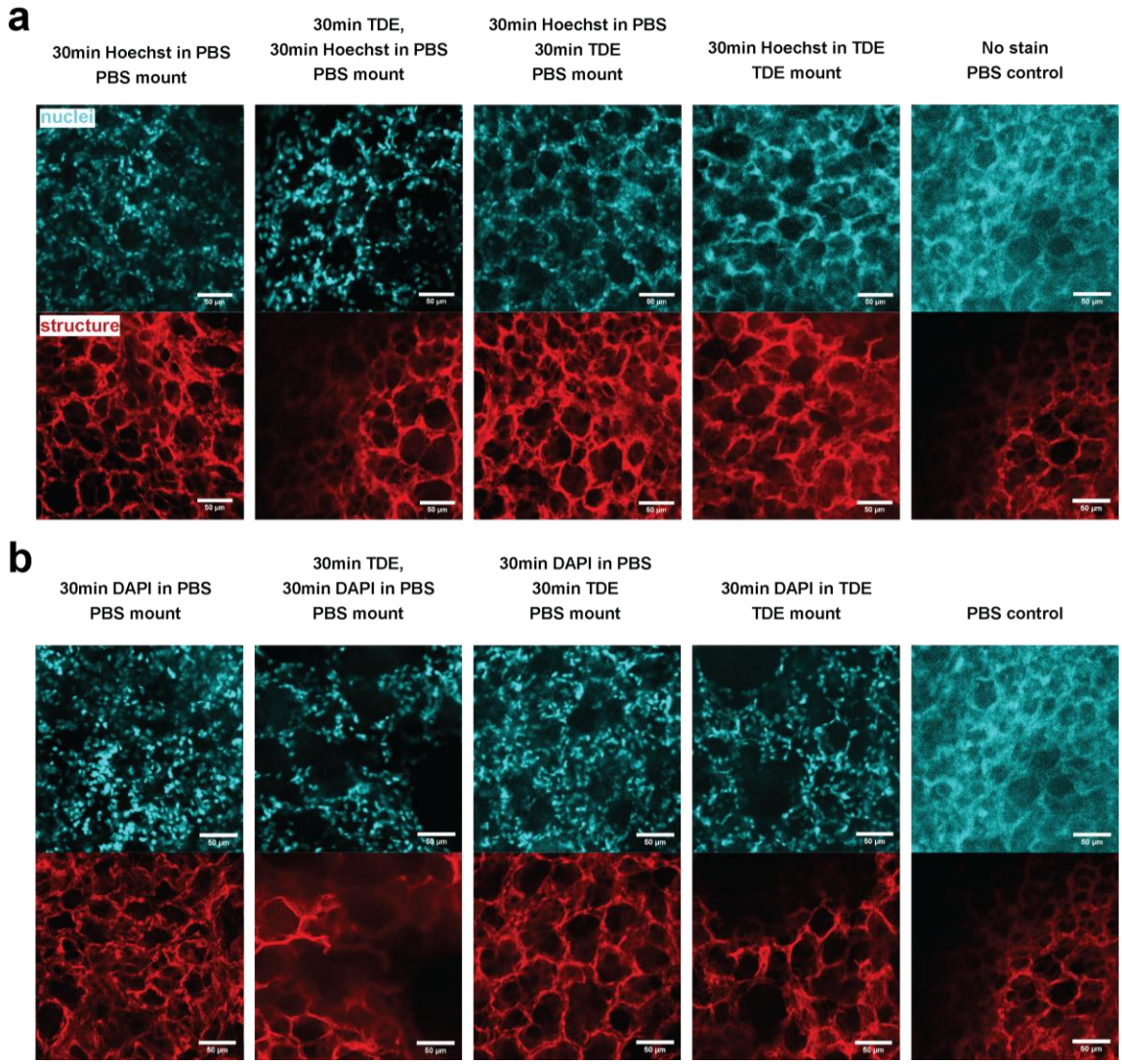

Figure 14: Effect of TDE clearing on nuclear staining fluorescence. (a) Hoechst 33342 fluorescence quenched following TDE clearing. (b) DAPI staining preserved nuclear fluorescence after clearing, providing a reliable nuclear label. Scale bars are 50 µm. The

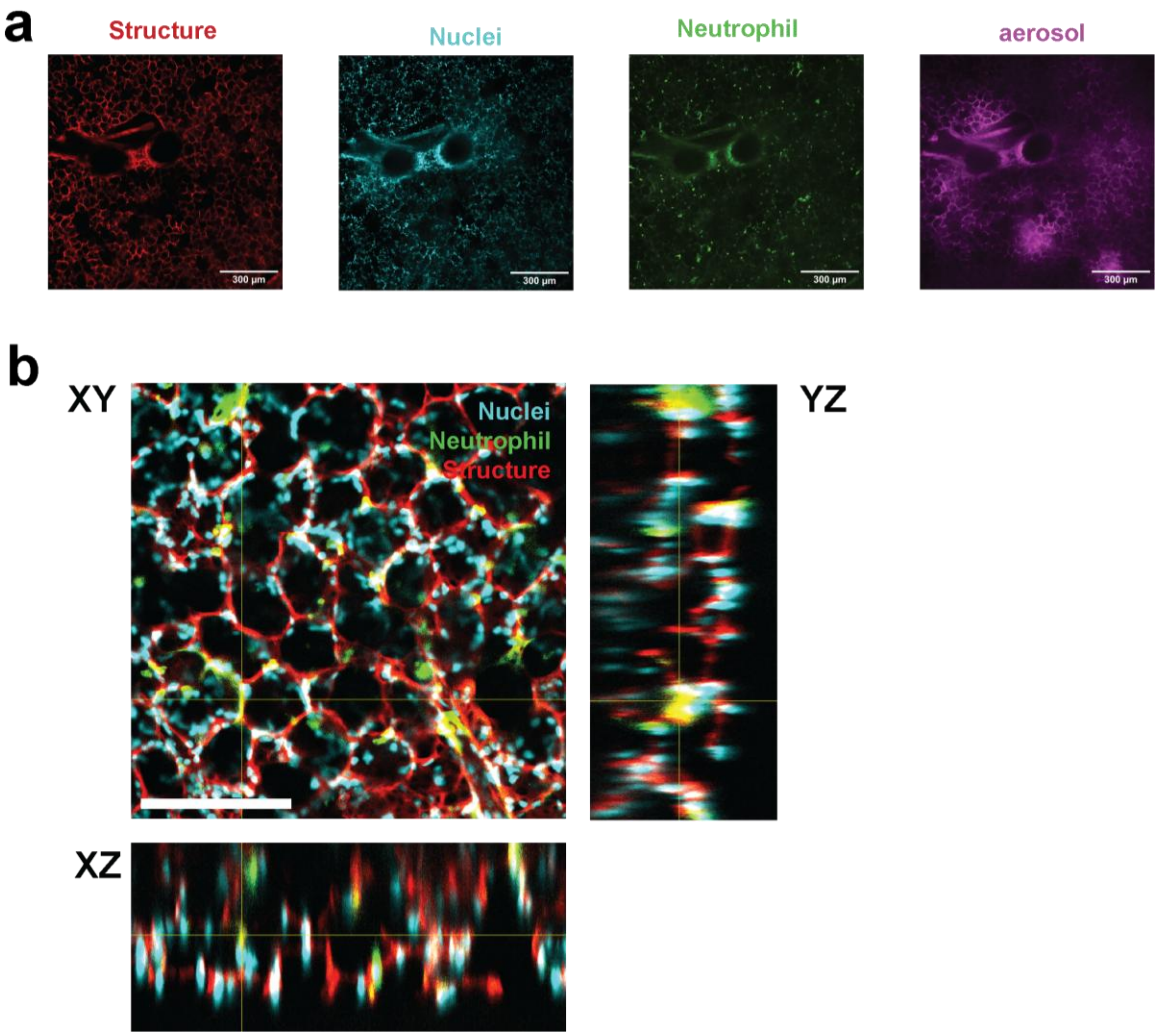

Figure 15: Visualization of cellular and structural features within a reconstructed lung volume. (a) Separate and tdTomato-labeled structure, DAPI-labeled nuclei, EGFP-expressing neutrophils, DiD aerosol label. (b) Composite XY and XZ views demonstrate multi-feature mapping with high lateral resolution.

Discussion

In this aim, we demonstrated that sequential slicing combined with OCT imaging offers a viable strategy for preserving structural integrity during volumetric reconstruction of the murine lung. Manual control-point registration enabled partial correction of slice deformations, and alignment to OCT volumes further improved anatomical fidelity. Additionally, we validated the imaging of fluorescent markers —

including nuclei, immune cells, and structural features — within thick cleared slices, establishing the compatibility of selected dyes with TDE clearing.

CONCLUSION AND FUTURE WORK

In conclusion, this thesis has established key components of an experimental pipeline for constructing a functional three-dimensional atlas of the murine lung, as outlined in Figure 16. In Aim 1, we developed optimized methods for lung sectioning, optical tissue clearing, and volumetric imaging using confocal microscopy, ensuring the preservation of alveolar and cellular resolution across large tissue volumes. In Aim 2, we addressed the challenges of image alignment by demonstrating that sequential slicing combined with optical coherence tomography (OCT) imaging provides a viable strategy for capturing an intact structural scaffold of the lung, facilitating the correction of slice deformations and enabling more anatomically accurate reconstructions.

Future work will focus on extending and refining this pipeline. This includes testing additional tissue clearing methods and imaging modalities to further improve optical transparency and resolution. A major goal will be the development of a multiplex immunofluorescent staining protocol compatible with optical clearing, enabling the sequential labeling and imaging of up to 40 molecular markers within the same lung volume. Additionally, scaling up computational pipelines for automated image alignment and reconstruction will be critical for assembling full-organ volumes containing many terabytes of data. Integrating structural reconstructions with functional models, such as airway network mapping and strain analysis, will ultimately allow the Functional Lung Atlas to serve as a comprehensive platform for studying lung structure, cellular

composition, and mechanical function across diverse physiological and pathological states.

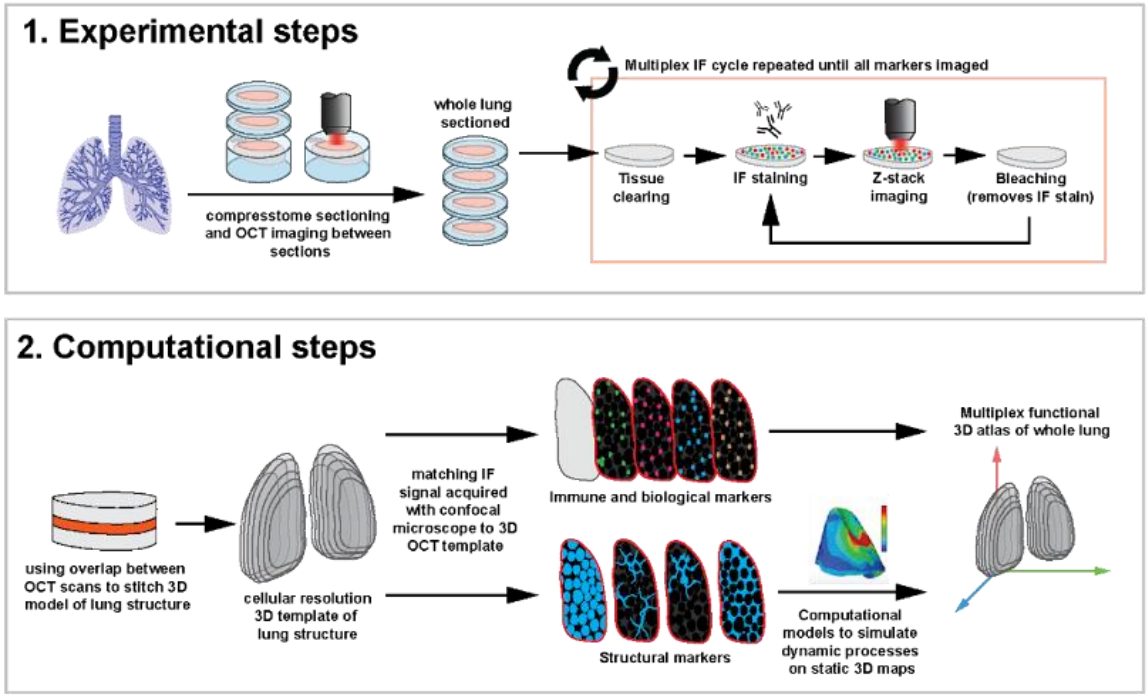

Figure 16: Schematic overview of the Functional Lung Atlas experimental pipeline. Workflow integrates sample preparation, clearing, imaging, alignment, and feature extraction for comprehensive 3D lung mapping.

BIBLIOGRAPHY

[1] Park, J., Wang, J., Guan, W., Gjesteby, L. A., Pollack, D., Kamentsky, L., Evans, N. B., Stirman, J., Gu, X., Zhao, C., Marx, S., Kim, M. E., Choi, S. W., Snyder, M., Chavez, D., Su-Arcaro, C., Tian, Y., Park, C. S., Zhang, Q., Yun, D. H., … Chung, K. (2024). Integrated platform for multiscale molecular imaging and phenotyping of the human brain. Science, 384(6701), eadh9979. https://doi.org/10.1126/science.adh9979

[2] Matuszak, J., Tabuchi, A., & Kuebler, W. M. (2020). Ventilation and Perfusion at the Alveolar Level: Insights From Lung Intravital Microscopy. Frontiers in Physiology, 11, 291. https://doi.org/10.3389/fphys.2020.00291

[3] Entenberg, D., Voiculescu, S., Guo, P., Borriello, L., Wang, Y., Karagiannis, G. S., Jones, J., Baccay, F., Oktay, M., & Condeelis, J. (2018). A permanent window for the murine lung enables high-resolution imaging of cancer metastasis. Nature Methods, 15(1), 73–80. https://doi.org/10.1038/nmeth.4511

[4] Sheng, W., Zhang, C., Mohiuddin, T. M., Al-Rawe, M., Zeppernick, F., Falcone, F. H., Meinhold-Heerlein, I., & Hussain, A. F. (2023). Multiplex immunofluorescence: A powerful tool in cancer immunotherapy. International Journal of Molecular Sciences, 24(4), 3086. https://doi.org/10.3390/ijms24043086

[5] Radtke, A. J., Chu, C. J., Yaniv, Z., Yao, L., Marr, J., Beuschel, R. T., Ichise, H., Gola, A., Kabat, J., Lowekamp, B., Speranza, E., Croteau, J., Thakur, N., Jonigk, D., Davis, J. L., Hernandez, J. M., & Germain, R. N. (2022). IBEX: an iterative immunolabeling and chemical bleaching method for high-content imaging of diverse tissues. Nature Protocols, 17(2), 378–401. https://doi.org/10.1038/s41596-021-00644-9

[6] Radtke, A. J., Kandov, E., Lowekamp, B., Speranza, E., Chu, C. J., Gola, A., Thakur, N., Shih, R., Yao, L., Yaniv, Z. R., Beuschel, R. T., Kabat, J., Croteau, J., Davis, J., Hernandez, J. M., & Germain, R. N. (2020). IBEX: A versatile multiplex optical imaging approach for deep phenotyping and spatial analysis of cells in complex tissues. Proceedings of the National Academy of Sciences of the United States of America, 117(52), 33455–33465. https://doi.org/10.1073/pnas.2018488117

[7] Lin, J. R., Fallahi‐Sichani, M., Chen, J. Y., & Sorger, P. K. (2016). Cyclic Immunofluorescence (CycIF), A Highly Multiplexed Method for Single-cell Imaging. Current Protocols in Chemical Biology, 8(4), 251–264. https://doi.org/10.1002/cpch.14

[8] Yapp, C., Nirmal, A. J., Zhou, F., Maliga, Z., Tefft, J. B., Llopis, P. M., Murphy, G. F., Lian, C. G., Danuser, G., Santagata, S., & Sorger, P. K. (2023). Multiplexed 3D Analysis of Immune States and Niches in Human Tissue. Cold Spring Harbor Laboratory. BioRxiv. https://dx.doi.org/10.1101/2023.11.10.566670

[9] Hsu, J., Nguyen, K. T., Bujnowska, M., Janes, K. A., & Fallahi-Sichani, M. (2024). Protocol for iterative indirect immunofluorescence imaging in cultured cells, tissue sections, and metaphase chromosome spreads. STAR Protocols, 5(3), 103190. https://doi.org/10.1016/j.xpro.2024.103190

[10] Park, J., Wang, J., Guan, W., Gjesteby, L. A., Pollack, D., Kamentsky, L., Evans, N. B., Stirman, J., Gu, X., Zhao, C., Marx, S., Kim, M. E., Choi, S. W., Snyder, M., Chavez, D., Su-Arcaro, C., Tian, Y., Park, C. S., Zhang, Q., Yun, D. H., … Chung, K. (2024). Integrated platform for multiscale molecular imaging and phenotyping of the human brain. Science, 384(6701), eadh9979. https://doi.org/10.1126/science.adh9979

[11] Kiemen, A. L., Braxton, A. M., Grahn, M. P., Han, K. S., Babu, J. M., Reichel, R., Jiang, A. C., Kim, B., Hsu, J., Amoa, F., Reddy, S., Hong, S. M., Cornish, T. C., Thompson, E. D., Huang, P., Wood, L. D., Hruban, R. H., Wirtz, D., & Wu, P. H. (2022). CODA: quantitative 3D reconstruction of large tissues at cellular resolution. Nature Methods, 19(11), 1490–1499. https://doi.org/10.1038/s41592-022-01650-9Clearing review

[12] Silvestri, L., Costantini, I., Sacconi, L., & Pavone, F. S. (2016). Clearing of fixed tissue: a review from a microscopist's perspective. Journal of Biomedical Optics, 21(8), 081205. https://doi.org/10.1117/1.JBO.21.8.081205

[13] Tian, T., Yang, Z., & Li, X. (2020). Tissue Clearing Technique: Recent progress and biomedical applications. Journal of Anatomy, 238(2), 489–507. https://doi.org/10.1111/joa.13309

[14] Susaki, E. A., & Ueda, H. R. (2016). Whole-body and whole-organ clearing and imaging techniques with single-cell resolution: Toward organism-level systems biology in mammals. Cell Chemical Biology, 23(1), 137–157. https://doi.org/10.1016/j.chembiol.2015.11.009

[15] Scott, G. D., Blum, E. D., Fryer, A. D., & Jacoby, D. B. (2014). Tissue optical clearing, three-dimensional imaging, and computer morphometry in whole mouse lungs and human airways. American Journal of Respiratory Cell and Molecular \Bbiology, 51(1), 43–55. https://doi.org/10.1165/rcmb.2013-0284OC

[16] Ochoa, L. F., Kholodnykh, A., Villarreal, P., Tian, B., Pal, R., Freiberg, A. N., Brasier, A. R., Motamedi, M., & Vargas, G. (2018). Imaging of Murine Whole Lung Fibrosis by Large Scale 3D Microscopy aided by Tissue Optical Clearing. Scientific Reports, 8(1), 13348. https://doi.org/10.1038/s41598-018-31182-2

[17] Yang, L., Feuchtinger, A., Möller, W., Ding, Y., Kutschke, D., Möller, G., Schittny, J. C., Burgstaller, G., Hofmann, W., Stoeger, T., Daniel Razansky, Walch, A., & Schmid, O. (2019). Three-Dimensional Quantitative Co-Mapping of Pulmonary

Morphology and Nanoparticle Distribution with Cellular Resolution in Nondissected Murine Lungs. ACS Nano, 13(2), 1029–1041. https://doi.org/10.1021/acsnano.8b07524

[18] Mzinza, D. T., Fleige, H., Laarmann, K., Willenzon, S., Ristenpart, J., Spanier, J., Sutter, G., Kalinke, U., Valentin-Weigand, P., & Förster, R. (2018). Application of light sheet microscopy for qualitative and quantitative analysis of bronchus-associated lymphoid tissue in mice. Cellular & Molecular Immunology, 15(10), 875–887. https://doi.org/10.1038/cmi.2017.150

[19] Erokhina, M. V., Lepekha, L. N., Voronezhskaya, E. E., Nezlin, L. P., Avdienko, V. G., & Ergeshov, A. E. (2019). Application of Laser Scanning Confocal Microscopy for the Visualization of M. tuberculosis in Lung Tissue Samples with Weak Ziehl-Neelsen Staining. Journal of Clinical Medicine, 8(8), 1185. https://doi.org/10.3390/jcm8081185

[20] LeBourdais, R., Grifno, G. N., Banerji, R., Regan, K., Suki, B., & Nia, H. T. (2024). Mapping the strain-stiffening behavior of the lung and lung cancer at microscale resolution using the crystal ribcage. Frontiers in Network Physiology, 4, 1396593. https://doi.org/10.3389/fnetp.2024.1396593

[21] Staudt, T., Lang, M.C., Medda, R., Engelhardt, J., Hell, S.W., 2007. 2,2′ - Thiodiethanol: A new water soluble mounting medium for high resolution optical microscopy. Microscopy Research and Technique 70, 1‐9. https://doi.org/10.1002/jemt.20396

[22] Costantini, I., Ghobril, J.-P., Di Giovanna, A. P., Mascaro, A. L., Silvestri, L., Müllenbroich, M. C., Onofri, L., Conti, V., Vanzi, F., Sacconi, L., Guerrini, R., Markram, H., Iannello, G., & Pavone, F. S. (2015). A versatile clearing agent for multi-modal brain imaging. Scientific Reports, 5(1). https://doi.org/10.1038/srep09808

[23] Aoyagi, Y., Kawakami, R., Osanai, H., Hibi, T., & Nemoto, T. (2015). A rapid optical clearing protocol using 2,2'-thiodiethanol for microscopic observation of fixed mouse brain. PLoS One, 10(1), e0116280. https://doi.org/10.1371/journal.pone.0116280

[24] Tian, T., Yang, Z., & Li, X. (2020). Tissue Clearing Technique: Recent progress and biomedical applications. Journal of Anatomy, 238(2), 489–507. https://doi.org/10.1111/joa.13309

[25] Chen, D., Segovia-Miranda, F., Walker, N., Valenzuela, J. I., Zerial, M., & Myers, E. W. (2020). Bridging scales in scattering tissues via multifocal two-photon microscopy. BioRxiv. https://doi.org/10.1101/2020.06.11.146704

[26] Ragan, T., Kadiri, L. R., Venkataraju, K. U., Bahlmann, K., Sutin, J., Taranda, J., Arganda-Carreras, I., Kim, Y., Seung, H. S., & Osten, P. (2012). Serial two-photon tomography for automated ex vivo mouse brain imaging. Nature Methods, 9(3), 255–258. https://doi.org/10.1038/nmeth.1854

[27] Seiriki, K., Kasai, A., Nakazawa, T., Niu, M., Naka, Y., Tanuma, M., Igarashi, H., Yamaura, K., Hayata-Takano, A., Ago, Y., & Hashimoto, H. (2019). Whole-brain block-face serial microscopy tomography at subcellular resolution using FAST. Nature Protocols, 14(5), 1509–1529. https://doi.org/10.1038/s41596-019-0148-4

[28] Soto, G. E., Young, S. J., Martone, M. E., Deerinck, T. J., Lamont, S., Carragher, B. O., Hama, K., & Ellisman, M. H. (1994). Serial section electron tomography: a method for three-dimensional reconstruction of large structures. NeuroImage, 1(3), 230–243. https://doi.org/10.1006/nimg.1994.1008

[29] Preibisch, S., Saalfeld, S., & Tomancak, P. (2009). Globally optimal stitching of tiled 3D microscopic image acquisitions. Bioinformatics, 25(11), 1463–1465. https://doi.org/10.1093/bioinformatics/btp184

[30] Chang, S., Yang, J., Novoseltseva, A., Fu, X., Li, C., Chen, S. C., Augustinack, J. C., Magnain, C., Fischl, B., Mckee, A. C., Boas, D. A., Chen, I. A., & Wang, H. (2023). Multi-Scale Label-free Human Brain Imaging with Integrated Serial Sectioning Polarization Sensitive Optical Coherence Tomography and Two-Photon Microscopy. BioRxiv : the preprint server for biology, 2023.05.22.541785. https://doi.org/10.1101/2023.05.22.541785

[31] Yang, J., Chang, S., Chen, I. A., Kura, S., Rosen, G. A., Saltiel, N. A., Huber, B. R., Varadarajan, D., Balbastre, Y., Magnain, C., Chen, S. C., Fischl, B., McKee, A. C., Boas, D. A., & Wang, H. (2022). Volumetric Characterization of Microvasculature in Ex Vivo Human Brain Samples by Serial Sectioning Optical Coherence Tomography. IEEE Transactions on Bio-medical Engineering, 69(12), 3645–3656. https://doi.org/10.1109/TBME.2022.3175072

CURRICULUM VITAE